Cai *et al. Clinical Proteomics* (2026) 23:29
https://doi.org/10.1186/s12014-026-09603-6

Clinical Proteomics

RESEARCH Open Access

Integrated serum proteomics and metabolomics reveal an INR-associated multi-omics signature in hepatocellular carcinoma

Yuying Cai[1†], Lingna Lyu[2†], Jiayi Ma[1], Xiaoru Wang[1], Wenxia Ma[2], Jiming Yin[1*] and Shanshan Wang[1*]

Abstract

Background Coagulation dysfunction is a common complication of hepatocellular carcinoma (HCC) and is reflected clinically by the international normalized ratio (INR), yet its serum molecular correlates remain poorly defined. We aimed to identify an INR-associated serum multi-omics signature in HCC and characterize the underlying molecular networks.

Methods We performed serum proteomics and untargeted metabolomics on 52 HCC patients and 30 healthy controls. HCC patients were stratified by INR levels. Differential molecules were integrated using pathway analysis. LASSO and logistic regression were used to derive an INR-associated multi-omics signature.

Results Proteomics and metabolomics identified 1,810 DEPs and 246 DEMs between HCC and controls. Integrated analysis mapped these changes to 101 shared pathways, highlighting cholesterol and central carbon metabolism. LASSO selected an eight-molecule signature comprising four proteins (CAMK2B, TGFB1, IDH1, LDHA) and four metabolites (DL-tryptophan, ornithine, D-glutamine, lysine) that discriminated INR-defined coagulation abnormality (AUC 0.859). WGCNA indicated remodeling of the coagulation-complement axis. In the TCGA-LIHC cohort, core genes were dysregulated, stratified overall survival, and showed partial concordance with INR status in an INR-annotated subset (AUC 0.668).

Conclusions Integrated serum proteomics and metabolomics revealed an INR-associated multi-omics signature and linked metabolic and immune–coagulation networks in HCC. These findings provide mechanistic insight and a candidate serum panel for future external validation.

Keywords hepatocellular carcinoma, INR, coagulation abnormality, proteomics, metabolomics

[†]Yuying Cai and Lingna Lyu contributed equally to this work.

*Correspondence:
Jiming Yin
yinjm7411@163.com
Shanshan Wang
wangshanshan1987@ccmu.edu.cn

[1]Beijing Institute of Hepatology, Beijing You'an Hospital, Capital Medical University, No. 8, Xitoutiao, Youanmenwai, Fengtai District, Beijing 100069, China
[2]Department of Gastroenterology and Hepatology, Beijing You'an Hospital, Capital Medical University, Beijing, China

Introduction

Liver cancer is the sixth most common malignant tumor globally and the third leading cause of cancer-related mortality [1]. China bears the heaviest burden of liver cancer, contributing 42.4% of all global cases [2]. The high mortality rate of hepatocellular carcinoma (HCC) is largely driven by late-stage diagnosis and the limitations of current imaging and serum biomarkers [3–8]. Serum is an ideal matrix for minimally invasive profiling of systemic pathophysiological states and for capturing molecular correlates of clinical phenotypes [9].

In recent years, high-throughput omics technologies, such as proteomics and metabolomics, have demonstrated significant potential for elucidating molecular mechanisms and phenotype-associated signatures for various diseases [10, 11]. These technologies enable the systematic mapping of global, molecular-level alterations associated with disease states [12]. However, in the field of HCC, despite existing single-omics studies [13, 14], integrated proteomics and metabolomics analyses of INR-defined coagulation abnormalities remain limited. Proteomics directly measures changes in protein abundance (the executors of biological activities), while metabolomics captures dynamic alterations in downstream small-molecule metabolites that serve as phenotypic endpoints [15, 16]. The integration of these two data layers allows for the construction of molecular regulatory networks that span from functional proteins to metabolic products, thereby providing a more comprehensive and profound understanding of the complex pathophysiological mechanisms of HCC [17, 18]. Rather than re-cataloging generic HCC-vs-HC differences, this study specifically focuses on INR-defined coagulopathy within HCC and uses integrated serum proteomics-metabolomics to map clinically anchored molecular networks.

Coagulation dysfunction in HCC presents a clinical paradox, characterized by a simultaneous risk of both severe bleeding and life-threatening thrombosis, which carries significant prognostic implications [19]. The risk of hemorrhage stems from the liver's central role in synthesizing coagulation factors; thus, progressive hepatic failure leads to reduced factor production and an elevated bleeding tendency [20]. Conversely, the tumor itself fosters a potent prothrombotic state. This is driven by multiple mechanisms, including the release of procoagulants like Tissue Factor (TF) that activate the extrinsic pathway, and the formation of tumor cell-platelet aggregates that facilitate immune evasion and promote metastasis [21]. This systemic hypercoagulability frequently culminates in major thrombotic events, most notably the formation of portal vein tumor thrombosis (PVTT)—a key determinant of poor prognosis [22]. Furthermore, the implications of this procoagulant state extend to the molecular level. Emerging evidence reveals a significant association between elevated coagulation activity and the upregulation of key immune checkpoint genes, such as PD-L1 and CTLA-4, suggesting that the coagulation system actively reshapes the tumor immune microenvironment and may thereby influence the efficacy of immunotherapy [23]. This dual threat of hemorrhage and thrombosis not only complicates clinical management but is also intrinsically linked to tumor progression, metastasis, and overall survival. Therefore, elucidating the molecular mechanisms of HCC-associated coagulation abnormalities and defining associated signatures are of critical clinical value for guiding personalized treatment and improving patient outcomes.

Therefore, this study was designed to characterize serum proteomic and metabolomic alterations in HCC and to derive an INR-associated multi-omics signature linked to coagulation abnormalities. We further investigated the molecular networks underlying this phenotype to provide mechanistic insight and a foundation for future validation.

Materials and methods

Patient cohorts and sample collection

The study cohort comprised 52 patients with a confirmed diagnosis of HCC and 30 healthy controls (HCs). All 52 HCC cases in this cohort were HBV-related and cirrhotic. The study protocol was approved by local Ethics Committees of Beijing You'an Hospital affiliated with Capital Medical University [No.2023023]. All procedures were conducted in full compliance with the Declaration of Helsinki. Written informed consent was obtained from each participant prior to enrollment. For each participant, peripheral venous blood was collected into a tube without anticoagulant. Samples were allowed to clot at room temperature for 30 min and were then centrifuged at 1,000 ×g for 10 min. The resulting serum was aliquoted and stored at − 80 °C until analysis. Detailed clinical characteristics of the HCC cohort are provided in Supplementary Table S1. Healthy-control samples were retrospectively obtained from the source clinical registry and designated as HC at sample collection. In this retrospective dataset, only age and sex metadata were available for HCs, and no additional prespecified inclusion/exclusion variables were available for re-analysis.

Untargeted serum metabolomics

Serum samples were extracted using pre-chilled methanol: acetonitrile (1:1, v/v) for protein precipitation. After centrifugation, supernatants were dried and reconstituted in acetonitrile: water (1:1, v/v). Untargeted metabolomics was performed by Shanghai Applied Protein Technology Co., Ltd. (APTBIO) on a Vanquish UHPLC system coupled to an Orbitrap Exploris 480 mass spectrometer (Thermo Scientific). Chromatographic

separation used an ACQUITY UPLC BEH Amide column (1.7 μm, 2.1 mm × 100 mm; Waters) at 25 °C with a flow rate of 0.5 mL/min and an injection volume of 2 μL. Mobile phases were A (water containing 25 mM ammonium acetate and 25 mM ammonia) and B (acetonitrile). The gradient was: 0–0.5 min, 95% B; 0.5–7 min, 95%-65% B; 7–8 min, 65%-40% B; 8–9 min, 40% B; 9–9.1 min, 40%-95% B; 9.1–12 min, 95% B. All samples were analyzed in a single analytical batch, with QC samples interspersed throughout the run to monitor instrument stability. MS data were acquired in both positive and negative ESI modes. Source settings were: sheath gas (Gas1) 50 arb, auxiliary gas (Gas2) 15 arb, sweep gas 2 arb, source temperature 350 °C, and spray voltage + 3,500 V/-2,800 V. For MS-only scans, the m/z range was 70-1200 with 60,000 resolution and 100 ms accumulation time. For auto MS/MS (segmented acquisition), the m/z range was 70-1200 with 60,000 resolution, 100 ms accumulation time, and dynamic exclusion of 4 s.

Serum proteomics

Low-abundance proteins were first enriched using magnetic beads (4 μL pre-washed beads per 100 μL serum/plasma; 2 h incubation, followed by wash steps). The bead-bound proteins were then denatured in UA buffer (8 M urea, 150 mM Tris-HCl, pH 8.0), reduced with DTT (final 20 mM, 60 min at 37 °C), alkylated with IAA (final 50 mM, 30 min at room temperature in the dark), diluted with 50 mM NH4HCO3 to reduce urea concentration to < 1.5 M, and digested with trypsin (1:50, w/w) for 16 h at 37 °C. Peptides were desalted on C18 cartridges, vacuum-concentrated, reconstituted in 0.1% formic acid, and spiked with iRT peptides. LC-MS/MS was performed on a Vanquish Neo UHPLC system coupled to an Orbitrap Astral mass spectrometer (Thermo Scientific). The analytical column was a Thermo Scientific EASY Column (15 cm × 150 μm ID, 2 μm; ES906). Mobile phase A was 0.1% formic acid in water, and mobile phase B was 0.1% formic acid in 80% acetonitrile/water. The injection amount was 400 ng, and the column temperature was 50 °C. Gradient program: 0.0–0.5 min, 4% B at 1.3 μL/min; 0.5–0.6 min, 4%-8% B (flow 1.3 to 0.8 μL/min); 0.6–0.9 min, 8%-8.5% B at 0.8 μL/min; 0.9–13.9 min, 8.5%-22.5% B at 0.8 μL/min; 13.9–20.8 min, 22.5%-35% B at 0.8 μL/min; 20.8–21.2 min, 35%-55% B (flow 0.8 to 2.0 μL/min); 21.2–21.7 min, 55%-99% B at 2.0 μL/min; 21.7–22.6 min, 99% B at 2.0 μL/min. MS1 scans covered m/z 380–980 at a resolution of 240,000. DIA acquisition used a fixed 2 Da isolation window with HCD collision energy of 25. The spray voltage was 1,900 V, and the ion transfer tube temperature was 280 °C. DIA raw files were processed using DIA-NN (v1.8.1), and identifications were filtered at 1% FDR (q < 0.01) at both the precursor level and protein-group level.

Bioinformatics analysis

Omics Data Analysis. For both metabolomics and proteomics, unsupervised Principal Component Analysis (PCA) was performed to visualize overall group separation. For metabolomics, differential metabolic features were screened using Variable Importance in Projection (VIP) > 1 from OPLS-DA and Student's t-test raw p-value < 0.05. Because this study was designed as an exploratory multi-omics analysis, raw p values were used only for initial feature screening in combination with effect-size criteria rather than as definitive statistical confirmation. Differentially expressed metabolites (DEMs) for downstream interpretation were defined as the annotated subset of significant features ($n = 246$) after matching to the in-house metabolite database. Fold change values were retained for effect-size reporting and volcano-plot visualization. Differentially expressed proteins (DEPs) were identified using the empirical Bayesian algorithm in the limma R package, with significance thresholds of fold change ≥ 1.5 (or ≤ 0.67) and raw p-value < 0.05. Gene Ontology (GO) and Kyoto Encyclopedia of Genes and Genomes (KEGG) pathway enrichment analyses were performed for DEPs and DEMs. For enrichment analyses in both omics layers, Benjamini-Hochberg (BH) correction was used to generate adjusted significance metrics (P.adj/FDR), which were reported alongside nominal p-values. For transparency, BH-adjusted p values for the HCC-vs-HC differential metabolite and protein tables were additionally calculated on the full tested datasets and are now provided in Supplementary Tables S2 and S3. A protein-protein interaction (PPI) network was constructed using the STRING database and visualized in Cytoscape.

Further, Weighted Gene Co-expression Network Analysis (WGCNA) was performed on the log2-transformed serum proteomic data from 52 HCC patients to identify co-expressed protein modules related to coagulation. A signed network was constructed with the WGCNA R package. The soft-thresholding power was determined based on the scale-free topology criterion (power = 14). A topological overlap matrix (TOM) was generated and subjected to average-linkage hierarchical clustering. The dynamic tree cut algorithm (minimum module size = 30) identified 12 colour-labelled modules. Module eigengenes (first principal components) were correlated with coagulation indices to explore module-trait relationships.

Integrated proteomic and metabolomic pathway analysis

An integrated pathway analysis was performed using the KEGG database to identify biological pathways commonly affected in HCC. DEPs and DEMs were subjected to KEGG pathway annotation and enrichment analysis in their respective omics layers, yielding 101 shared pathways by intersection. For pathway reporting, both

nominal p-values and adjusted significance values (P.adj/FDR) were retained. For biological prioritization, four pathways were selected based on nominal enrichment in both layers (raw $p < 0.05$ in proteomic and metabolomic enrichment) together with biological relevance to HCC/coagulation biology. DEPs and DEMs were also co-mapped onto the central carbon metabolism in cancer pathway diagram to visualize coordinated molecular changes.

Construction of an INR-associated Multi-omics signature

The HCC cohort was stratified into an INR-defined coagulation abnormality group (INR > 1.2, $n = 21$) and a normal coagulation group (INR ≤ 1.2, $n = 31$). A Least Absolute Shrinkage and Selection Operator (LASSO) regression analysis was performed on the combined proteomic and metabolic data to select features associated with INR status. The optimal regularization parameter (lambda) was determined via 10-fold cross-validation. A logistic regression model was then constructed using the selected features to summarize group discrimination. Because no independent external serum cohort was available, model performance in Fig. 5E represents internal apparent performance in the same 52-patient derivation cohort. To reduce overfitting risk, we used penalized feature selection (LASSO), cross-validated lambda selection, and a parsimonious final model (8 molecules), and we explicitly interpret the results as hypothesis-generating pending external validation. A two-sided p-value < 0.05 was considered statistically significant for all analyses.

Transcriptomic concordance analysis using the TCGA-LIHC cohort

Transcriptomic concordance analysis was conducted using RNA-sequencing (STAR counts) and clinical data from The Cancer Genome Atlas Liver Hepatocellular Carcinoma (TCGA-LIHC) project. Raw data and clinical information were accessed via the TCGAbiolinks R/Bioconductor package. For a more detailed analysis of INR-defined coagulation abnormality, an enhanced clinical dataset containing INR values for 294 HCC patients was obtained from cBioPortal. Differential gene expression between HCC ($n = 374$) and non-tumor tissues ($n = 50$) was assessed using the Wilcoxon rank-sum test. For survival analysis, patients were stratified into high- and low-expression groups based on the median expression of each gene, and Kaplan–Meier curves were compared using the log-rank test. A multivariable Cox proportional hazards model combining the four core genes (CAMK2B, TGFB1, IDH1, LDHA) was constructed to compute a composite risk score. Tumor–normal discrimination was evaluated by ROC curve analysis using univariate and multivariate logistic regression models, and AUC values were calculated with the pROC package. In the INR-annotated subset, patients were classified into an INR-defined coagulation abnormality group (INR > 1.2, $n = 113$) and a normal coagulation group (INR ≤ 1.2, $n = 181$). The ability of the 4-gene model to discriminate INR status was evaluated using the same statistical framework.

Statistical analysis

Clinical and Statistical Analysis. Clinical characteristics were analyzed using SPSS 22.0 (IBM Corp.) and R. For HC-vs-HCC baseline comparison, age was compared by the Mann-Whitney U test and sex by Fisher exact test. For INR-stratified HCC comparisons, continuous variables were compared by the Mann-Whitney U test, and categorical variables were compared using Chi-square or Fisher exact tests as appropriate. For differential screening, metabolomic features were selected by VIP > 1 with raw $p < 0.05$, and proteomic DEPs were selected by fold change ≥ 1.5 (or ≤ 0.67) with raw $p < 0.05$. These molecule-level screening criteria were used for exploratory discovery rather than stand-alone confirmatory inference. For enrichment analyses in both omics layers, Benjamini-Hochberg (BH) correction was used and adjusted values (P.adj/FDR) were reported. In the integrative pathway-prioritization step, four pathways were prioritized using nominal significance in both layers (raw $p < 0.05$ in both proteomic and metabolomic enrichment) plus biological relevance. All tests were two-sided, and $p < 0.05$ was considered statistically significant unless otherwise specified.

Results

Clinical characteristics of the study population

The study design and analysis workflow is illustrated in Fig. 1. The study included 52 HCC patients and 30 HCs, and baseline characteristics are summarized in Table 1. Sex distribution did not differ significantly between groups (19/30 vs. 40/52 males, $P = 0.210$), whereas patients with HCC were significantly older than HCs (58.49 ± 10.43 vs. 35.83 ± 9.75 years, $P < 0.0001$). Detailed HCC clinical characteristics are provided in Supplementary Table S1. All HCC cases in this cohort were HBV-related and cirrhotic (52/52 each; Supplementary Table S1).

The metabolic components of the HCC and HC groups were distinct

Multivariate analysis of metabolic profiles revealed distinct clustering patterns between HCC patients and HC. PCA demonstrated clear separation of metabolic phenotypes between the HCC and HC groups (Fig. 2A). QC samples interspersed throughout the analytical sequence clustered tightly in the overall PCA space, supporting good instrument stability and arguing against

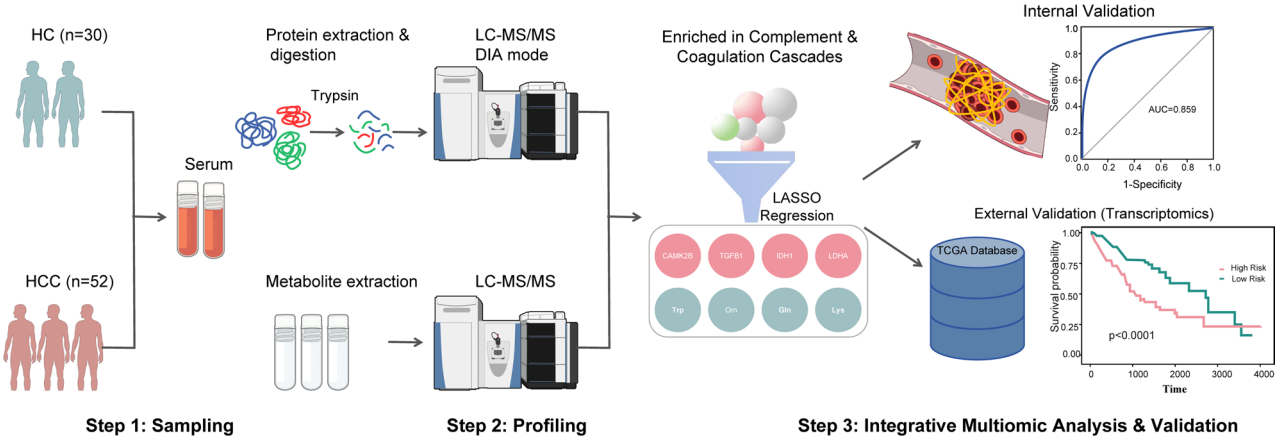

Fig. 1 Proteomics and metabolomics analysis workflow for HC and HCC patients. The study design consists of three steps: (1) Sampling of serum from healthy controls (HC, $n=30$) and hepatocellular carcinoma patients (HCC, $n=52$); (2) multi-omics profiling using LC-MS/MS for protein and metabolite identification; and (3) integrative analysis, LASSO feature selection, and transcriptomic concordance analysis. An INR-associated panel comprising four proteins and four metabolites was derived. Abbreviations: Trp, tryptophan; Orn, ornithine; Gln, glutamine; Lys, lysine; CAMK2B, calcium/calmodulin-dependent protein kinase II beta; TGFB1, transforming growth factor beta 1; IDH1, isocitrate dehydrogenase 1; LDHA, lactate dehydrogenase A

Table 1 Baseline characteristics of healthy controls and patients with HCC

Characteristic	HC ($n=30$)	HCC ($n=52$)	*P* value*
Sample size, n	30	52	
Age, years (mean ± SD)	35.83 ± 9.75	58.49 ± 10.43	< 0.0001
Age, years (median [IQR])	36.00 [27.50, 42.75]	59.00 [52.50, 65.00]	
Male, n (%)	19 (63.3%)	40 (76.9%)	0.210
Female, n (%)	11 (36.7%)	12 (23.1%)	

*Age was compared using the Mann-Whitney U test. Sex distribution was compared using Fisher exact test

major batch/order effects. Within the HC samples, PCA still suggested a potential internal two-subgroup trend; because HC metadata were limited to age/sex in this retrospective dataset, this pattern could not be further resolved by available covariates and was interpreted as likely inter-individual heterogeneity. Screening based on VIP > 1 and $p < 0.05$ identified 1,095 differential metabolic features. Among these differential features, 246 annotated metabolites were retained as DEMs for downstream analyses (Fig. 2C). Of these, 233 remained significant after BH correction in the full HCC-vs-HC feature set, and the corresponding adjusted p values are now provided in Supplementary Table S3. Volcano plot analysis was used to visualize fold-change patterns of metabolic features (Fig. 2B). Notably, metabolites displaying both high fold changes (FC > 2.0) and elevated variable importance in projection (VIP > 1) scores were prioritized as potential biomarkers (Fig. 2D). Pathway enrichment analysis through KEGG mapping revealed significant perturbation of 114 metabolic pathways, with 16 pathways meeting nominal significance (raw $p < 0.05$) (Fig. 2E); adjusted significance values (P.adj/FDR) are reported in enrichment outputs. The most prominently dysregulated pathways (enrichment factor > 2.5) centered on neoplastic metabolic reprogramming, particularly in choline metabolism in cancer ($p = 1.06 \times 10^{-3}$) and cholesterol homeostasis pathways ($p = 6.97 \times 10^{-4}$). Core pathway-network analysis identified three key hubs of metabolic disruption: (1) antifolate resistance mechanisms, (2) aminoacyl-tRNA biosynthesis, and (3) ABC transporter activity, all exhibiting extensive connectivity with multiple DEMs (Fig. 2F). Of particular clinical relevance, we observed marked alterations in rate-limiting metabolites of hepatic choline metabolism (3-hydroxybutyric acid showed a 2.72-fold increase) and bile acid synthesis (Glycochenodeoxycholic acid showed a 116-fold increase). Full annotated DEM results are provided in Supplementary Table S3.

The protein components of the HCC and HC groups were distinct

To provide context for downstream INR-associated analyses, we implemented a DIA-MS platform for comprehensive serum proteome profiling and compared HCC patients with healthy controls. A total of 2,402 protein groups were quantified. PCA demonstrated distinct proteomic signatures differentiating HCC patients from HCs (Fig. 3A). Significant separation between groups was demonstrated through hierarchical clustering (Fig. 3B). Quantitative analysis identified DEPs. The volcano plot highlighted 1,482 up-regulated and 328 down-regulated proteins (fold change > 1.5 or < 0.67, $p < 0.05$) (Fig. 3C). The butterfly plot revealed substantial protein expression differences, identifying FGG, FGB, and RSU1 as among the most upregulated, and CFP, APCS, and HYDIN as among the most downregulated (Fig. 3D). After BH correction in the full HCC-vs-HC protein dataset, 1,801

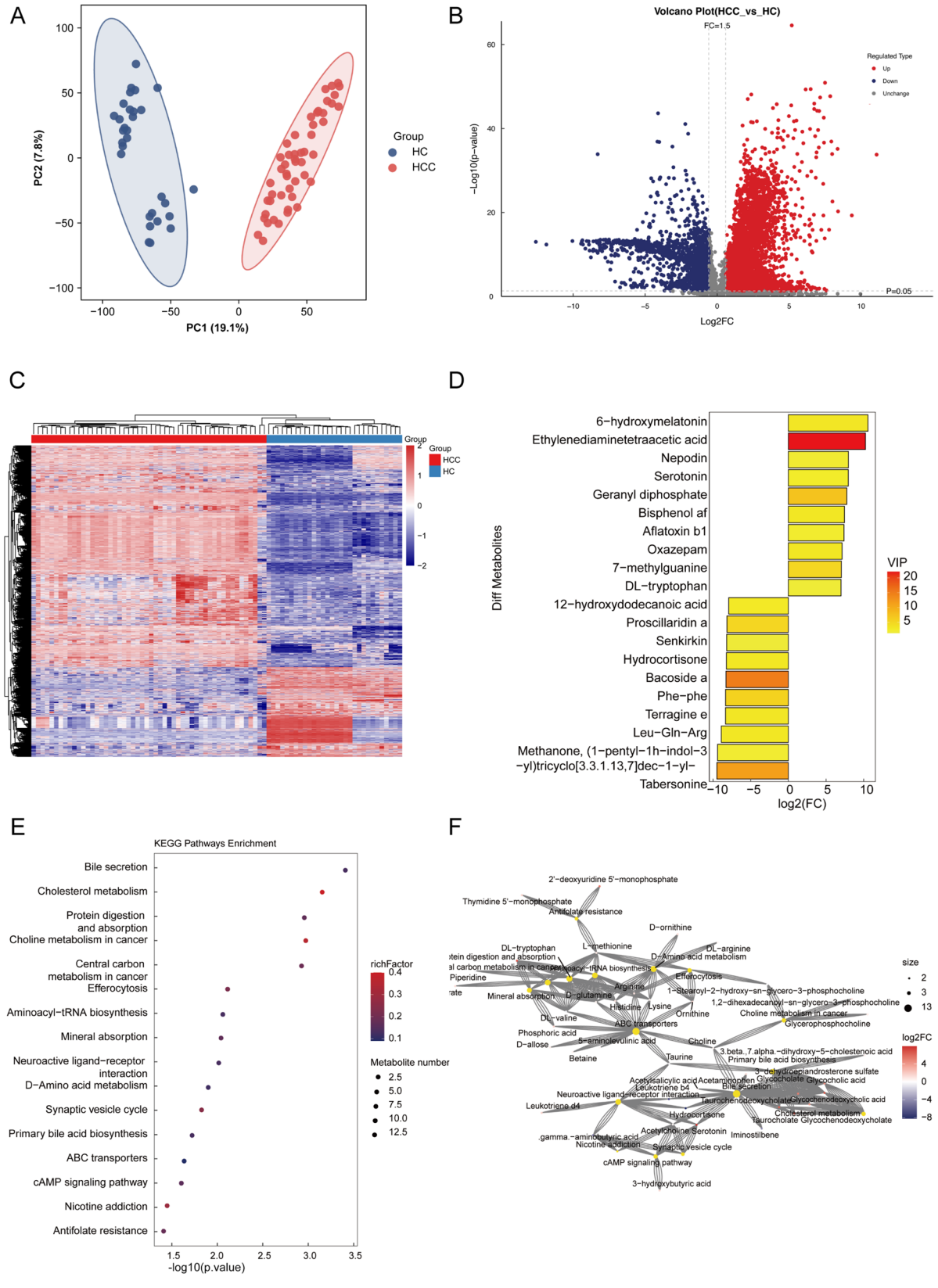

Fig. 2 Serum Metabolomics Analysis in HCC and HC. (**A**) PCA of metabolomic data in HCC and HC. (**B**) Volcano plot of HCC vs. HC metabolites. (**C**) Heatmap of DEMs. (**D**) Bar chart of the top-ranked DEMs by fold change and VIP score. (**E**) Bubble plot of KEGG enrichment analysis of DEMs. (**F**) Correlation network of strongly associated DEMs

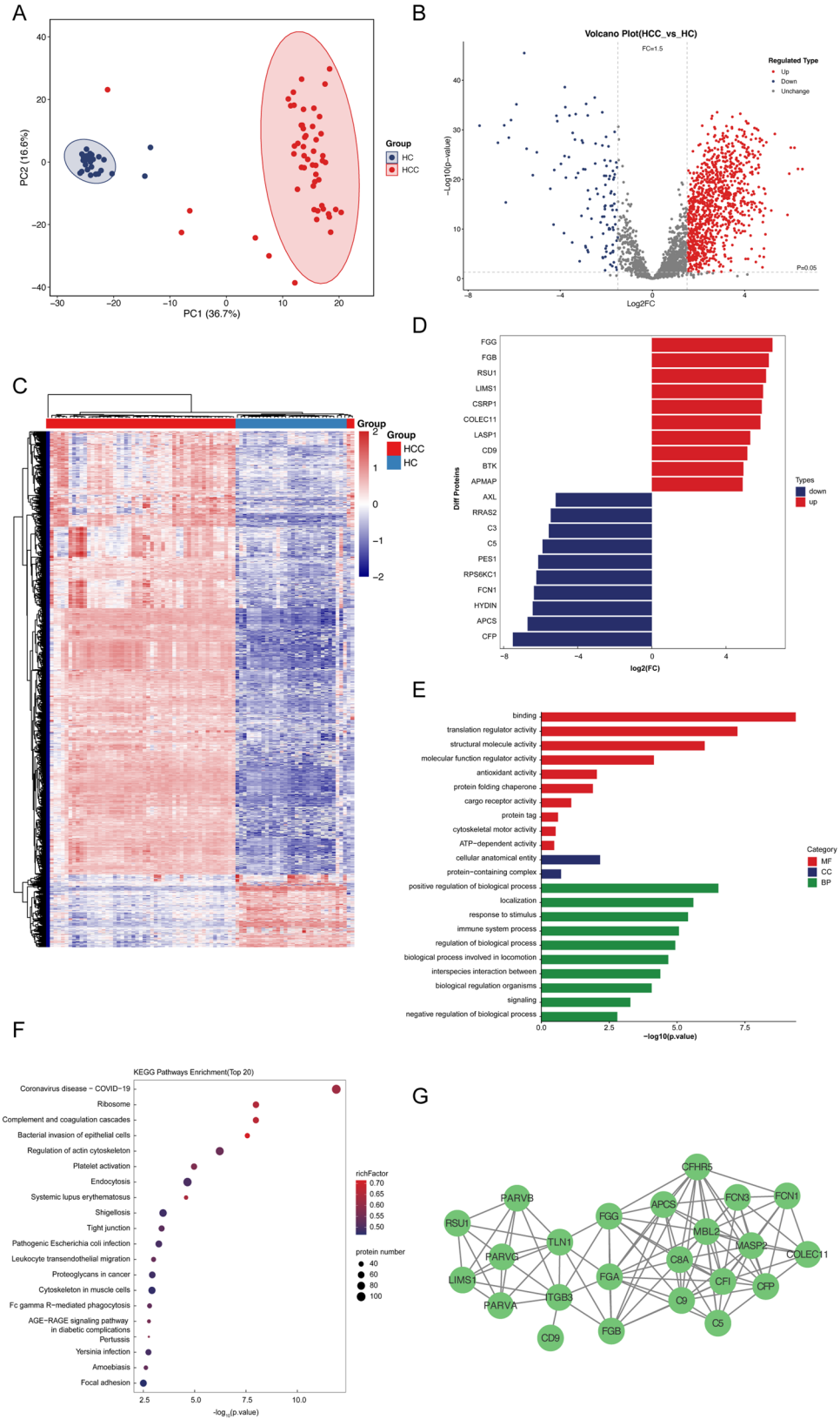

Fig. 3 Serum Proteomics Analysis in HCC and HC. A total of 2,402 protein groups were quantified. (**A**) PCA of HCC and HC proteomics data. (**B**) Hierarchical clustering heatmap of serum proteomic profiles. (**C**) Volcano plot of HCC vs. HC proteins. (**D**) Butterfly plot showing top upregulated and downregulated proteins. (**E**) GO enrichment analysis of DEPs. (**F**) KEGG enrichment analysis of DEPs. (**G**) Protein-protein interaction network

of the 1,810 DEPs remained significant, and the corresponding adjusted p values are now provided in Supplementary Table S2.

To elucidate the pathophysiological relevance of these DEPs, GO enrichment analysis revealed predominant molecular functions in ligand-binding domains and translational regulation, coupled with biological processes involving positive regulation of cellular processes and intracellular transport mechanisms (Fig. 3E). These functional characteristics implicate dysregulated signal transduction networks, translational reprogramming, and immune microenvironment remodeling as critical components of hepatocarcinogenesis. KEGG pathway analysis identified a total of 48 nominally enriched pathways (raw $p < 0.05$), with adjusted significance values (P.adj/FDR) reported in enrichment outputs. The top 20 most significantly enriched pathways are displayed (Fig. 3F), with ribosome biogenesis, complement activation cascade, and coagulation cascade being the most prominently associated.

Protein interaction network topology analysis identified CFHR5, CFP, and C9 as central network hubs (degree centrality > 15), with MBL2 and other complement components forming dense interaction modules (Fig. 3G).

Integrated metabolomics and proteomics analysis of HCC patients

The previous results showed significant changes in serum metabolome and proteome in HCC patients compared with healthy controls. To further analyze the association between these changes, we performed integrative pathway analyses using 246 annotated DEMs and 1,810 DEPs as input sets. Pathway analysis was performed at both protein and metabolite levels with KEGG annotation. A Venn plot showed 101 shared pathways across the two omics layers (Fig. 4A). The KEGG bubble map displays

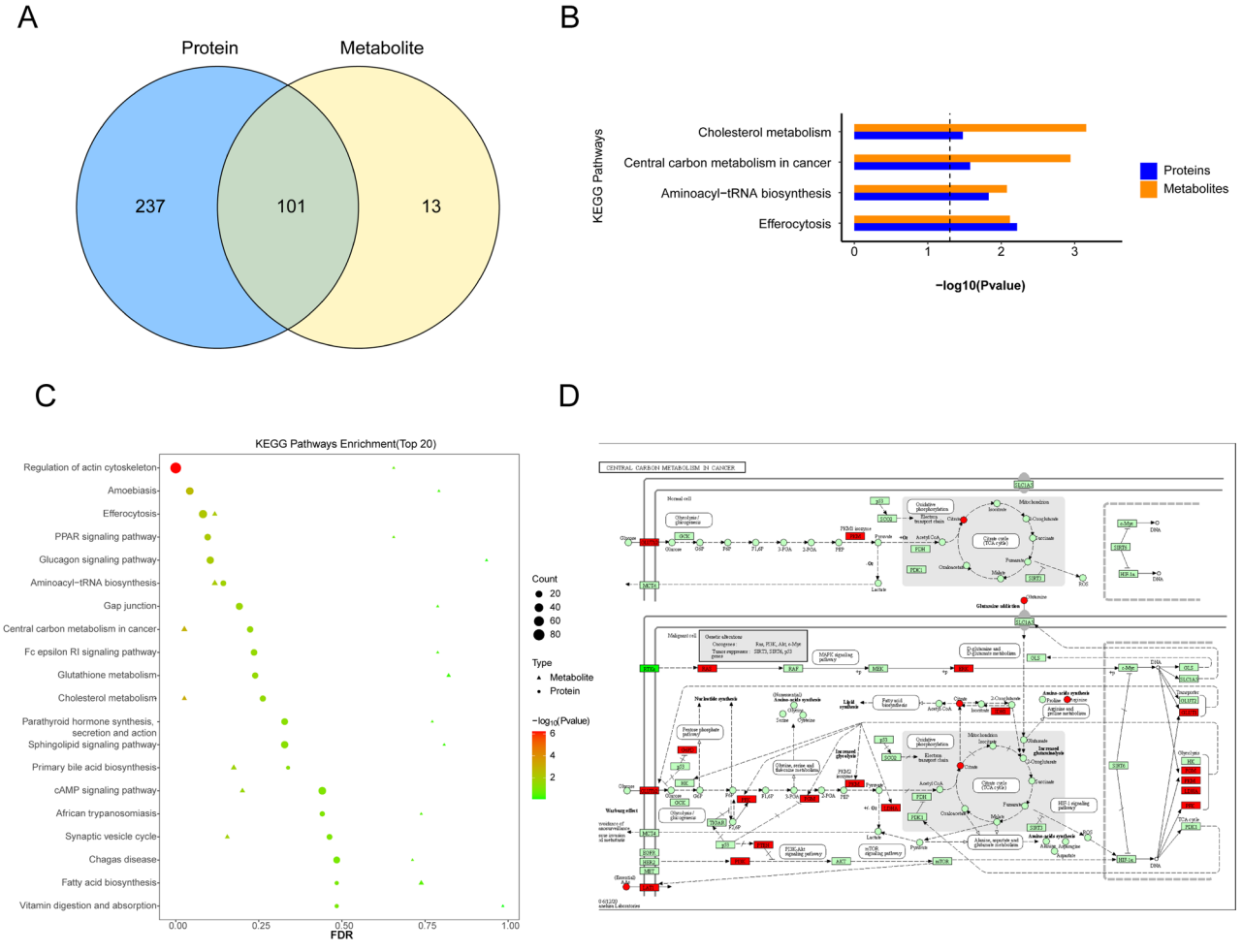

Fig. 4 Integrated Analysis of Metabolomics and Proteomics. (**A**) Venn diagram showing shared KEGG pathways between metabolomic and proteomic enrichment results (101 shared pathways). (**B**) Bubble plot of the top 20 shared pathways. (**C**) Prioritized four pathways with nominal enrichment in both omics layers (raw $p < 0.05$ in proteomic and metabolomic enrichment): cholesterol metabolism, central carbon metabolism in cancer, aminoacyl-tRNA biosynthesis, and efferocytosis. (**D**) Representative co-mapping of proteins and metabolites in central carbon metabolism in cancer (red, up-regulated; green, down-regulated)

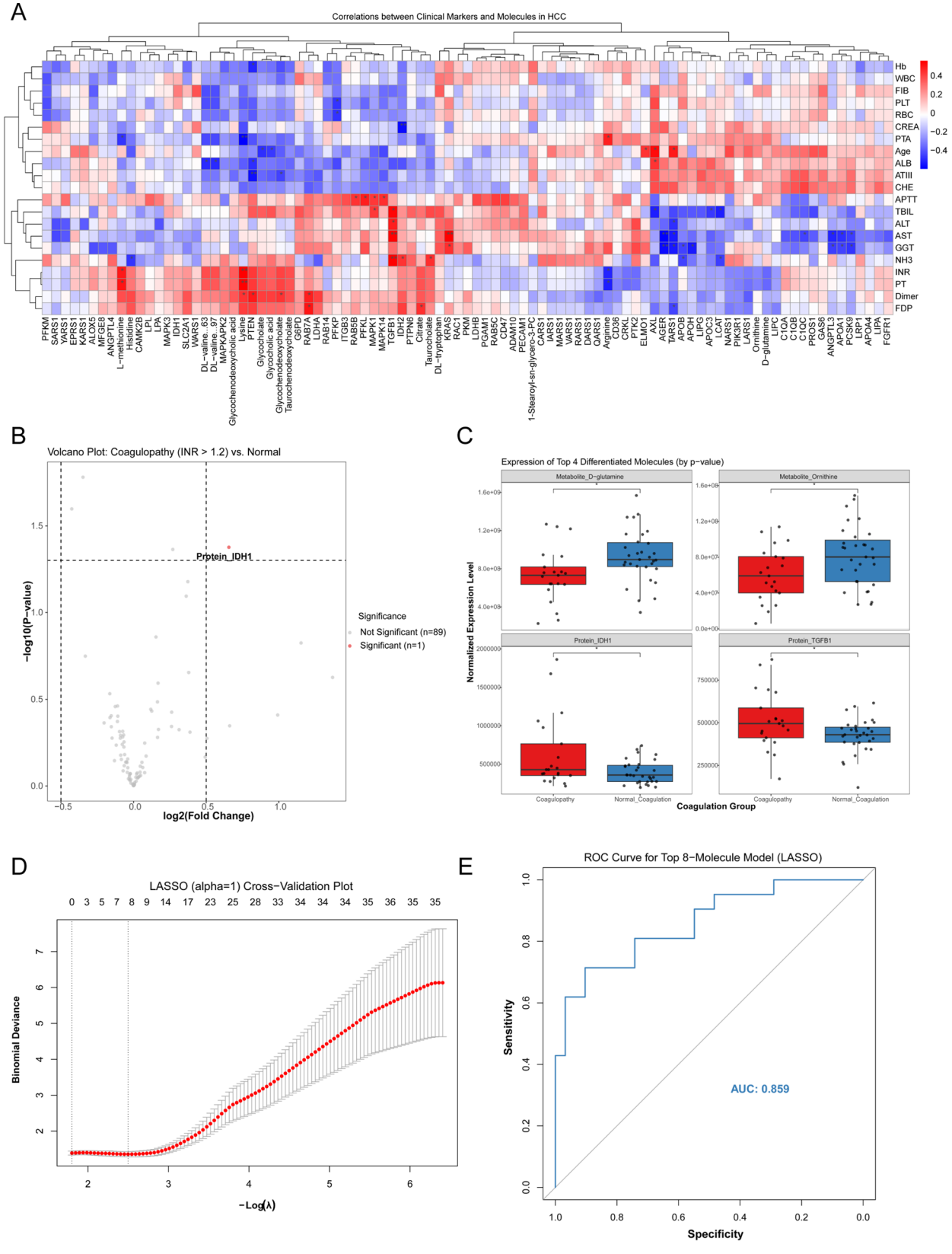

Fig. 5 (See legend on next page.)

(See figure on previous page.)

Fig. 5 Multi-omics Signature Associated with INR-Defined Coagulation Abnormality in HCC. (**A**) Correlation heatmap of key molecules and clinical parameters. Red indicates positive correlation, blue indicates negative correlation. (**B**) Volcano plot of molecules in the INR-defined coagulation abnormality vs. normal coagulation groups. (**C**) Box plots of the top four differential molecules (IDH1, TGFB1, D-glutamine, Ornithine) between the two groups. (**D**) LASSO regression analysis for feature selection, identifying an 8-molecule signature. (**E**) ROC curve analysis of the 8-molecule signature for distinguishing INR-defined coagulation abnormality

the top 20 shared pathways (Fig. 4B). For biological prioritization, we focused on four pathways showing nominal enrichment in both layers (raw $p < 0.05$ in proteomic and metabolomic enrichment) and clear biological relevance: cholesterol metabolism, central carbon metabolism in cancer, aminoacyl-tRNA biosynthesis, and efferocytosis (Fig. 4C). The KEGG pathway diagram further illustrates core protein and metabolite alterations in central carbon metabolism in cancer (Fig. 4D).

Derivation of an INR-associated multi-omics signature

To systematically investigate the association between key molecules identified from the integrated analysis and clinical phenotypes of HCC, we first generated a correlation heatmap of these molecules against hematological parameters (Fig. 5A). The results revealed that the molecular profiles exhibited complex clustering patterns with the clinical indices. Notably, a subset of metabolites (e.g., kynurenine, tryptophan) and proteins (e.g., MAPK14, PFKL) displayed strong positive correlations (red clusters) with markers of liver injury (ALT, AST) and coagulation (INR, PT), whereas other molecules showed negative correlations (blue clusters). This finding suggests that systemic alterations in the proteome and metabolome are intimately linked to the clinicopathological status of HCC patients, particularly INR-defined coagulation abnormality.

Prompted by these findings, we focused on INR-defined coagulation abnormality. We stratified the cohort of 52 HCC patients into an INR-defined coagulation abnormality group (INR > 1.2, $n = 21$) and a normal coagulation group (INR ≤ 1.2, $n = 31$) based on INR. Clinical characteristics of the two groups are summarized in Table 2. After collapsing BCLC stages into early stage (A) versus intermediate/advanced stages (B-D), the INR > 1.2 group showed a higher proportion of intermediate/advanced disease than the INR ≤ 1.2 group (61.9% vs. 29.0%, Fisher exact $P = 0.024$). Volcano plot analysis revealed that, at the defined threshold ($p < 0.05$, $|\log2FC| > 0.5$), protein IDH1 was the sole molecule exhibiting statistically significant upregulation in the INR-defined abnormality group (Fig. 5B). To further explore potential markers, we visualized the top four molecules ranked by p-value; box plots illustrated the expression levels of protein IDH1, protein TGFB1, D-glutamine, and ornithine between the two groups (Fig. 5C). The results confirmed the significant elevation of IDH1 and revealed a consistent upward trend for the other three molecules, suggesting their association with this phenotype.

To derive a multi-molecule INR-associated signature, we employed the LASSO regression algorithm to select the most informative feature set from the high-dimensional data at the optimal lambda value (Fig. 5D). The LASSO cross-validation ultimately identified a signature comprising eight molecules: four proteins (CAMK2B, TGFB1, IDH1, LDHA) and four metabolites (DL-tryptophan, ornithine, D-glutamine, lysine). A logistic regression model constructed based on this 8-molecule signature discriminated INR-defined coagulation abnormality (AUC = 0.859; Fig. 5E). As this was an internal derivation cohort without independent external serum validation, this AUC is interpreted as internal apparent performance.

WGCNA identifies coagulation and complement modules in HCC serum

WGCNA analysis of the serum proteome identified 12 distinct co-expression modules (Fig. 6A). Sample clustering confirmed the absence of significant outliers, and a soft-thresholding power of 14 was selected to ensure scale-free topology (Supplementary Figure S1). While module eigengenes showed modest linear correlations with INR (Fig. 6B), we prioritized three modules heavily populated by the previously identified DEPs. The brown module (containing 210 DEPs) was enriched for complement activation (e.g., C9, C8A, MBL2; Fig. 6C). The black module (42 DEPs) focused on coagulation regulation, clustering fibrinogens (FGA, FGB, FGG), coagulation factors (F7, F11), and plasminogen (Fig. 6D). The blue module (323 DEPs) reflected broad immune and extracellular matrix responses, including C3, C1Q complex, and properdin (Fig. 6E). A focused heatmap of coagulation- and complement-related DEPs from the black, brown and blue modules demonstrated coordinated expression changes in fibrinogen chains, coagulation factors and complement components between HCC and HCs and across INR strata (Fig. 6F). All these findings provided a network-level view of the coagulation–complement axis in this cohort.

Transcriptomic concordance of the core gene components in the TCGA-LIHC cohort

To explore tissue-level concordance of the four core proteins (CAMK2B, TGFB1, IDH1, LDHA) derived from the eight-molecule signature, we analyzed RNA-sequencing

Table 2 Clinical characteristics of HCC patients stratified by INR

Characteristic	INR ≤ 1.2 (*n* = 31)	INR > 1.2 (*n* = 21)	*P* value
Sample size, n	31	21	
Sex: Male, n (%)	25 (80.6%)	15 (71.4%)	0.512
Sex: Female, n (%)	6 (19.4%)	6 (28.6%)	
BCLC: Early stage (A), n (%)	22 (71.0%)	8 (38.1%)	0.024
BCLC: Intermediate/Advanced stages (B-D), n (%)	9 (29.0%)	13 (61.9%)	
AFP, median [IQR]	9.48 [2.77, 97.45]	7.45 [2.40, 280.75]	0.764
Age, median [IQR]	58.50 [53.25, 61.00]	60.00 [52.00, 68.00]	0.314
WBC, median [IQR]	3.56 [2.96, 5.06]	4.03 [1.81, 6.00]	0.852
RBC, median [IQR]	3.80 [3.07, 4.17]	2.79 [2.68, 3.81]	0.024
Hb, median [IQR]	120.00 [94.00, 131.00]	92.00 [70.00, 117.00]	0.016
PLT, median [IQR]	88.00 [57.00, 135.50]	67.00 [47.00, 82.00]	0.088
NH3, median [IQR]	66.50 [47.50, 83.25]	71.00 [42.00, 93.50]	0.820
ALT, median [IQR]	29.00 [16.50, 38.00]	28.00 [18.00, 43.00]	1.000
AST, median [IQR]	34.00 [23.50, 44.50]	37.00 [25.00, 71.00]	0.318
TBIL, median [IQR]	23.50 [16.85, 30.35]	29.70 [20.70, 56.40]	0.023
ALB, median [IQR]	36.00 [32.95, 39.75]	30.80 [27.60, 35.60]	0.001
GGT, median [IQR]	42.00 [25.50, 124.50]	44.00 [26.00, 106.00]	0.970
CHE, median [IQR]	4045.00 [2786.00, 6047.50]	2045.00 [1452.00, 3566.00]	0.004
CREA, median [IQR]	70.00 [61.50, 86.50]	57.00 [54.00, 67.00]	0.022
PT, median [IQR]	10.05 [9.62, 10.47]	12.30 [11.60, 15.70]	< 0.001
PTA, median [IQR]	75.60 [69.70, 79.25]	56.20 [45.00, 59.10]	< 0.001
INR, median [IQR]	1.10 [1.06, 1.14]	1.33 [1.26, 1.55]	< 0.001
APTT, median [IQR]	37.80 [34.40, 40.15]	45.80 [40.00, 51.40]	< 0.001
FIB, median [IQR]	2.58 [2.29, 3.08]	1.76 [1.29, 2.21]	< 0.001
Dimer, median [IQR]	1.00 [0.20, 2.10]	2.30 [1.40, 4.10]	0.009
FDP, median [IQR]	4.67 [0.68, 10.08]	8.24 [5.39, 12.51]	0.097
ATIII, median [IQR]	70.20 [61.15, 78.15]	46.10 [35.20, 54.20]	< 0.001
AFP missing, n (%)	1 (3.2%)	5 (23.8%)	

Data are presented as n (%) or median [IQR]. For BCLC stage, categories were collapsed into Early stage (A) versus Intermediate/Advanced stages (B-D); P value was calculated by Fisher exact test (2 × 2). Continuous variables were compared using the Mann-Whitney U test. Categorical variables were compared using Chi-square/Fisher exact test as appropriate

and clinical data from the TCGA-LIHC cohort. Comparison of 374 primary liver tumors and 50 normal liver tissues revealed that CAMK2B, LDHA and TGFB1 were significantly dysregulated in tumor tissues (Fig. 7A).

Further, the prognostic value and tumor–normal discrimination of these genes were evaluated by univariate Kaplan–Meier analysis and ROC analysis. The results showed that high expression of LDHA was significantly associated with shorter overall survival, whereas the other three genes displayed non-significant trends (Supplementary Figure S2). A multivariable Cox model combining all four genes yielded a composite risk score that stratified patients into high- and low-risk groups with highly divergent overall survival (Fig. 7B). In tumor–normal discrimination, CAMK2B exhibited the highest single-gene performance (AUC = 0.831; Supplementary Figure S3), and a multivariable logistic regression model integrating all four genes achieved an AUC of 0.811 for distinguishing tumor from normal tissues in the TCGA-LIHC cohort (Fig. 7C).

To evaluate whether the 4-gene signature captures INR-associated biology, we leveraged an enhanced TCGA clinical dataset containing INR values for 294 HCC patients. Patients were stratified into an INR-defined coagulation abnormality group (INR > 1.2, $n = 113$) and a normal coagulation group (INR ≤ 1.2, $n = 181$). Expression levels of IDH1, CAMK2B and LDHA were significantly increased in the INR-defined abnormality group (Fig. 7D). A logistic regression model based on the 4-gene signature achieved an AUC of 0.668 for distinguishing INR-defined coagulation abnormality from normal coagulation status (Fig. 7E), indicating partial concordance across matrices.

Discussion

This study combined non-targeted serum proteomics with metabolomics to characterise the molecular landscape of HCC and to derive an INR-associated multi-omics signature of coagulation abnormality. By integrating protein and metabolite profiles, we identified an eight-molecule serum panel comprising four proteins (CAMK2B, TGFB1, IDH1, LDHA) and four metabolites (DL-tryptophan, ornithine, D-glutamine, lysine) that discriminated INR-defined groups with good accuracy (AUC = 0.859). These findings highlight serum multi-omics as a mechanistic window into INR-defined coagulation abnormality in HCC rather than a definitive diagnostic test.

Independent omics analyses revealed significant molecular alterations in HCC patients. Metabolomics data indicated that tumors induce systemic metabolic reprogramming characterized by the overlap of impaired liver function and tumor metabolic demands. For instance, glycocholic acid levels increased 116-fold, reflecting severe dysfunction in hepatic bile acid handling and suggesting that accumulated bile acids may act as pro-cancer signaling molecules that drive tumor proliferation and invasion [24]. Notably, our finding of elevated glycocholic acid is consistent with a large multicenter study involving nearly 1,500 participants, which identified glycocholic acid and phenylpyruvate as effective metabolic biomarkers for early-stage HCC [25]. Concurrently, activation of pathways such as choline metabolism and aminoacyl-tRNA biosynthesis indicates increased demand for membrane and protein synthesis substrates to support rapid tumor-cell proliferation [26]. Proteomics analysis further

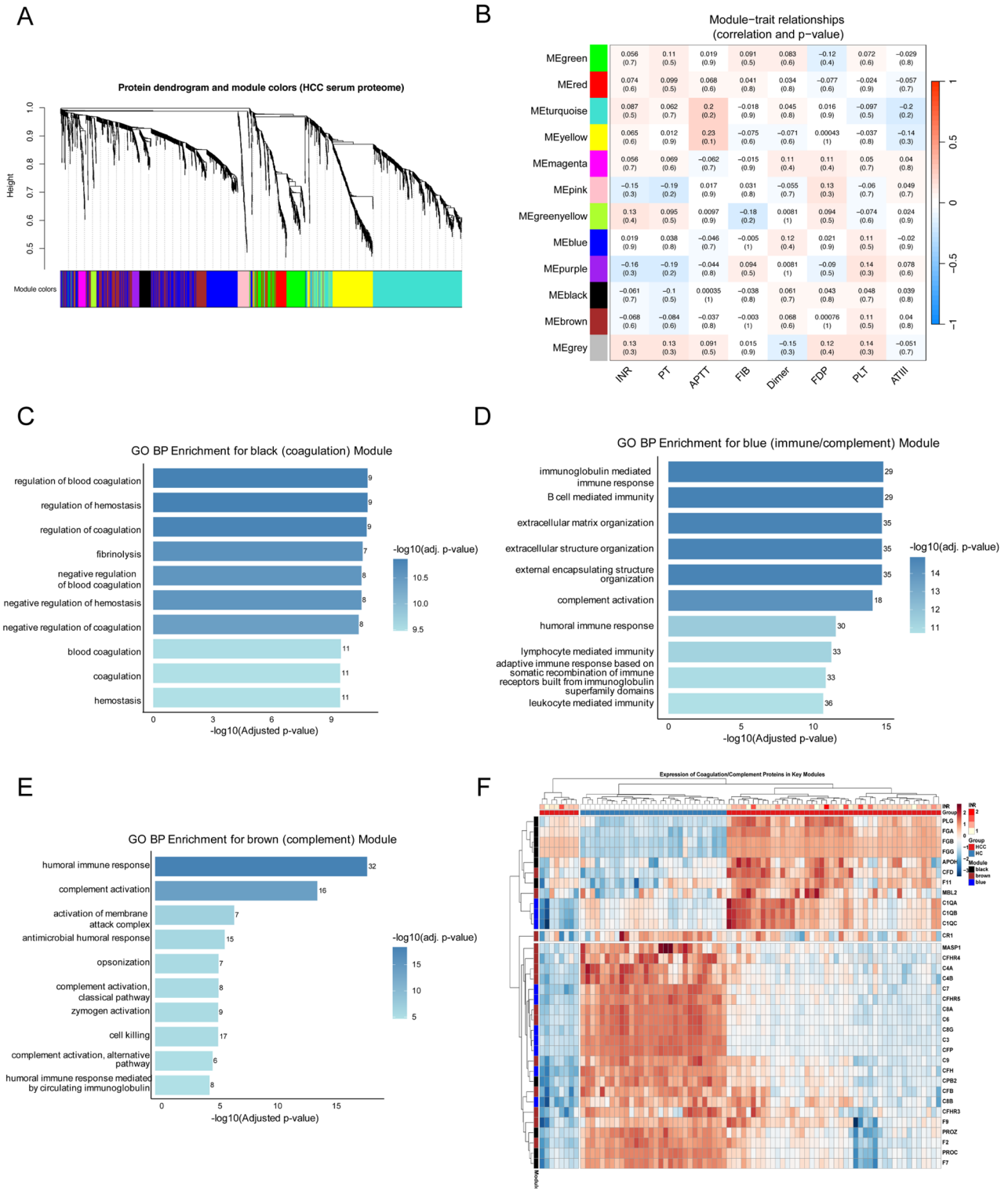

Fig. 6 Co-expression Network Analysis of the HCC Serum Proteome. (**A**) Dendrogram of 2,402 serum proteins based on topological overlap, with 12 WGCNA modules indicated by color bars. (**B**) Heatmap of correlations between module eigengenes and coagulation indices (INR, PT, APTT, FIB, D-dimer, FDP, PLT, ATIII). (**C-E**) GO biological process enrichment for DEPs in the brown (complement), black (coagulation), and blue (immune/complement) modules. (**F**) Heatmap of coagulation- and complement-related DEPs belonging to the black, brown, and blue modules across HCC patients and healthy controls, with columns annotated by group and INR status

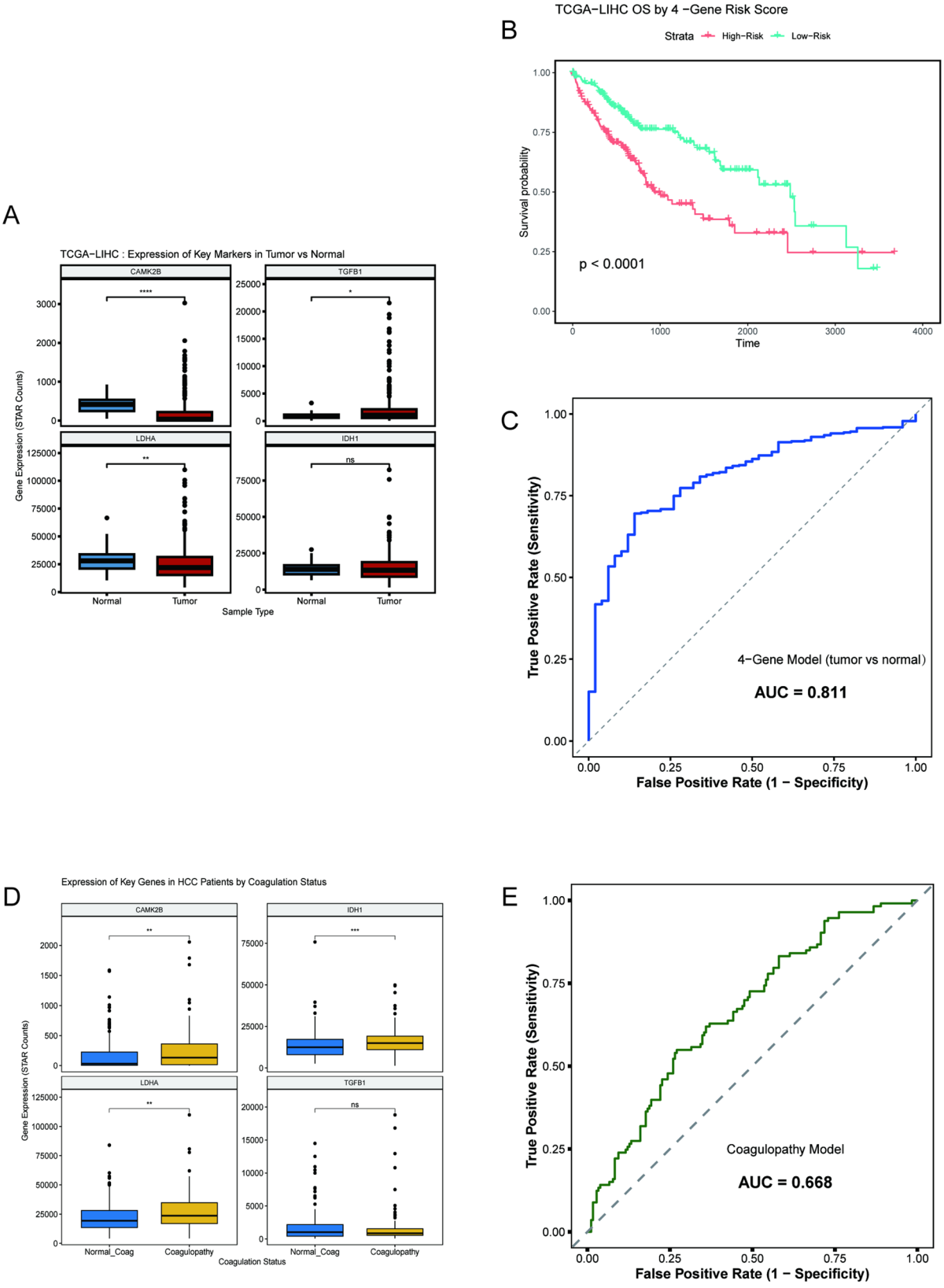

Fig. 7 (See legend on next page.)

(See figure on previous page.)

Fig. 7 Transcriptomic concordance of the 4-gene signature in the TCGA-LIHC cohort. (**A**) Box plots showing differential expression of CAMK2B, IDH1, LDHA and TGFB1 between tumour ($n = 374$) and normal ($n = 50$) liver tissues in TCGA-LIHC. (**B**) Kaplan–Meier curves for overall survival in TCGA-LIHC patients stratified by the composite 4-gene risk score (high- vs. low-risk groups). (**C**) ROC curve for a multivariable 4-gene logistic regression model distinguishing tumour from normal tissues. (**D**) Box plots comparing expression of the four genes between HCC patients with INR-defined coagulation abnormality (INR > 1.2, $n = 113$) and those with normal coagulation (INR ≤ 1.2, $n = 181$) in the INR-annotated subset. (**E**) ROC curve for the 4-gene model in distinguishing INR-defined coagulation abnormality status (INR > 1.2 vs. ≤ 1.2) in TCGA-LIHC

revealed adaptive changes in host response. Upregulation of coagulation-related proteins such as fibrinogen (FGG, FGB) and disruption of the complement system (e.g., CFP) pointed to chronic inflammation and a hypercoagulable state in HCC patients [27]. Crucially, WGCNA showed that these were coordinated dysregulations rather than isolated events; identification of distinct coagulation modules supports the coagulation-complement axis. This axis involves key proteins such as SERPIND1, F12, and KNG1, and was confirmed as a critical enriched pathway in HCC [14, 28].

The key innovation of this study lies in applying multi-omics integration in a clinically anchored, INR-oriented framework within HCC, rather than only reporting generic HCC-vs-HC differences. A recent review indicates that multi-omics strategies have successfully mapped over ten key pathways in HCC [29, 30]. We identified 101 pathways co-disturbed at both the protein and metabolite levels, demonstrating that the observed changes represent a highly synergistic systemic dysregulation. A prominent example is the complement and coagulation cascade pathway. Our integrated analysis revealed significant alterations in this pathway at both the proteomic and metabolomic levels. This finding aligns with another multi-omics study, which similarly demonstrated that proteomics and metabolomics data collectively point to activation of this pathway, providing a molecular-level explanation for the INR-defined coagulation phenotype observed in HCC patients [31]. Furthermore, alteration in central carbon metabolism in cancer exemplifies this phenomenon. We observed not only upregulation of key enzymes involved in glycolysis and the tricarboxylic acid cycle (e.g., LDHA, IDH1), but also concurrent alterations in the concentrations of their downstream metabolites (e.g., D-glutamine). This synchronized change in proteins and metabolites demonstrates activation of the Warburg effect in HCC, revealing how protein expression changes ultimately lead to metabolic phenotype remodeling [32].

Coagulation dysfunction is a critical issue affecting HCC patient prognosis, yet traditional indicators like INR provide limited mechanistic insight [33]. Our study shows that the identified differentially expressed molecules correlate with clinical coagulation markers (INR, PT), supporting biologically relevant links. Considering the limitations of single biomarkers, we used LASSO regression to identify an optimal molecular combination from integrated protein-metabolite data. The final panel of eight molecular biomarkers encompasses core pathological pathways revealed in prior analyses: IDH1 and LDHA represent dysregulated central carbon metabolism [34, 35]; TGFB1 and CAMK2B involve liver fibrosis and signal transduction [36, 37]; while ornithine, D-glutamine, lysine, and DL-tryptophan reflect disturbances in amino acid metabolism, the urea cycle, and the immune microenvironment [38, 39]. In TCGA-LIHC, core genes were dysregulated and a gene-based score stratified overall survival; the INR-annotated subset showed modest discrimination (AUC 0.668), consistent with partial cross-matrix concordance and emphasizing the need for external serum validation.

This study employed an integrated proteomics and metabolomics strategy to reveal key molecular networks associated with INR-defined coagulation abnormality in HCC serum. Limitations include the single-center cohort, modest sample size, and the lack of independent serum validation and targeted assays; TCGA provides only tissue-level concordance. In addition, healthy-control metadata were limited to age/sex in this retrospective dataset, which constrained investigation of potential residual heterogeneity (including the apparent HC subgrouping pattern in unsupervised projections). Furthermore, as all enrolled HCC patients were HBV-related and had underlying cirrhosis and our study lacked an independent, non-HCC cirrhosis control group, the current 8-molecule signature is specifically an indicator of coagulopathy within HCC, and its utility for discriminating benign cirrhosis from HCC cannot be determined. In addition, because molecule-level feature screening initially used raw p values in combination with effect-size criteria, residual false-positive findings may remain at the individual-molecule level; therefore, these results should be interpreted as exploratory and hypothesis-generating pending independent external validation. Future studies should validate this signature in external serum cohorts and by targeted proteomics/metabolomics, and clarify causal mechanisms through functional experiments. Nevertheless, these results provide a mechanistic framework and candidate markers for further evaluation.

Conclusions

Integrated serum proteomics and metabolomics identified an INR-associated multi-omics signature that reflects coordinated metabolic and immune-coagulation network

remodeling in HCC. These findings provide mechanistic insight and candidate serum markers that require validation in independent external cohorts.

Abbreviations

AUC	Area under the curve
DEMs	Differentially expressed metabolites
DEPs	Differentially expressed proteins
DIA	Data-independent acquisition
FDR	False discovery rate
GO	Gene ontology
HC	Healthy controls
HCC	Hepatocellular carcinoma
INR	International normalized ratio
KEGG	Kyoto Encyclopedia of Genes and Genomes
LASSO	Least absolute shrinkage and selection operator
LC-MS/MS	Liquid chromatography-tandem mass spectrometry
OPLS-DA	Orthogonal partial least-squares discriminant analysis
PCA	Principal component analysis
PPI	Protein–protein interaction
PVTT	Portal vein tumor thrombosis
ROC	Receiver operating characteristic
TCGA-LIHC	The cancer genome atlas liver hepatocellular carcinoma
TF	Tissue factor
VIP	Variable importance in projection
WGCNA	Weighted gene co-expression network analysis

Supplementary Information

The online version contains supplementary material available at https://doi.org/10.1186/s12014-026-09603-6.

Supplementary material 1.

Supplementary material 2.

Supplementary material 3.

Supplementary material 4.

Acknowledgements
Not applicable.

Author contributions
J.Y. and S.W. conceived and designed the study. Y.C. was responsible for sample collection, data analysis, and drafting the manuscript. L.L. provided clinical samples and interpreted the clinical data. J.M., X.W., and W.M. assisted in sample collection and data curation. J.Y. and S.W. supervised the study and revised the manuscript critically. All authors read and approved the final manuscript.

Funding
This work was supported by the National Natural Science Foundation of China (Grant No. 82372260), the Beijing YouAn Hospital Construction of Talent Pool Program (Grant No. YARCKB2023003), the Demonstrating Application and Research of Clinical Diagnosis and Treatment Technology in Beijing (Grant No. Z221100007422002), and the Sino-German Mobility Programme (Grant No. M-0200).

Data availability
The mass spectrometry proteomics data have been deposited to the ProteomeXchange Consortium (https://proteomecentral.proteomexchange.org) via the iProX partner repository with the dataset identifier PXD074800 (iProX project ID: IPX0014955000). During peer review, the dataset is available via private share access: [https://www.iprox.cn/page/SSV024.html; url=1770869641888DgYj] (Password: [SmQA]). The untargeted metabolomics data are available in the OMIX repository, China National Center for Bioinformation, under accession number OMIX014059 (https://ngdc.cncb.ac.cn/omix).

Declarations

Ethics approval and consent to participate
The study protocol was approved by the local Ethics Committees of Beijing You'an Hospital affiliated with Capital Medical University [No.2023023]. Written informed consent was obtained from each participant.

Consent for publication
Not applicable.

Competing interests
The authors declare no competing interests.

Received: 12 February 2026 / Accepted: 1 April 2026
Published online: 19 April 2026

References

1. Sung H, et al. Global Cancer Statistics 2020: GLOBOCAN Estimates of Incidence and Mortality Worldwide for 36 Cancers in 185 Countries. CA Cancer J Clin. 2021;71(3):209–49.
2. Chan SL, et al. The Lancet Commission on addressing the global hepatocellular carcinoma burden: comprehensive strategies from prevention to treatment. Lancet. 2025;406(10504):731–78.
3. Anwanwan D, et al. Challenges in liver cancer and possible treatment approaches. Biochim Biophys Acta Rev Cancer. 2020;1873(1):188314.
4. Chan Y, et al. Biomarkers for diagnosis and therapeutic options in hepatocellular carcinoma. Mol Cancer. 2024;23(1):189.
5. Kim DH, et al. Comparison of non-contrast abbreviated MRI and ultrasound as surveillance modalities for HCC. J Hepatol. 2024;81(3):461–70.
6. Wang M, et al. Conversion therapy for advanced hepatocellular carcinoma in the era of precision medicine: Current status, challenges and opportunities. Cancer Sci. 2024;115(7):2159–69.
7. Kim DY, et al. Utility of combining PIVKA-II and AFP in the surveillance and monitoring of hepatocellular carcinoma in the Asia-Pacific region. Clin Mol Hepatol. 2023;29(2):277–92.
8. Hanif H, et al. Update on the applications and limitations of alpha-fetoprotein for hepatocellular carcinoma. World J Gastroenterol. 2022;28(2):216–29.
9. Pinero F, Dirchwolf M, Pessoa MG. Biomarkers in Hepatocellular Carcinoma: Diagnosis, Prognosis and Treatment Response Assessment. Cells, 2020. 9(6) 1370.
10. So JBY, et al. Development and validation of a serum microRNA biomarker panel for detecting gastric cancer in a high-risk population. Gut. 2021;70(5):829–37.
11. He B, et al. miRNA-based biomarkers, therapies, and resistance in Cancer. Int J Biol Sci. 2020;16(14):2628–47.
12. Reel PS, et al. Using machine learning approaches for multi-omics data analysis: A review. Biotechnol Adv. 2021;49:107739.
13. Hou G, et al. Metabolomics-based classification reveals subtypes of hepatocellular carcinoma. Mol Carcinog. 2022;61(11):989–1001.
14. Tsai T, et al. LC-MS/MS-based serum proteomics for identification of candidate biomarkers for hepatocellular carcinoma. Proteomics. 2015;15(13):2369–81.
15. Ding Z, et al. Proteomics technologies for cancer liquid biopsies. Mol Cancer. 2022;21(1):53.
16. Wishart DS. Metabolomics for Investigating Physiological and Pathophysiological Processes. Physiol Rev. 2019;99(4):1819–75.
17. Dubin RF, Rhee EP. Proteomics and Metabolomics in Kidney Disease, including Insights into Etiology, Treatment, and Prevention. Clin J Am Soc Nephrol. 2020;15(3):404–11.
18. Navas-Carrillo D, et al. High-resolution proteomics and metabolomics in thyroid cancer: Deciphering novel biomarkers. Crit Rev Clin Lab Sci. 2017;54(7–8):446–57.
19. Azam A et al. Role of Coagulation Factors in Hepatocellular Carcinoma: A Literature Review. Life (Basel), 2024. 15(1) 34.
20. Stotts MJ, Davis JPE, Shah NL. Coagulation testing and management in liver disease patients. Curr Opin Gastroenterol. 2020;36(3):169–76.
21. Qu G, et al. Integrated analysis and experimental validation reveal the prognostic and immunological features associated with coagulation in hepatocellular carcinoma. Sci Rep. 2025;15(1):8626.

22. La Mura V, et al. The management of liver disease in people with congenital bleeding disorders: guidance from European Association for Haemophilia and Allied Disorders, European Haemophilia Consortium, ISTH, and World Federation of Hemophilia. J Thromb Haemost. 2024;22(12):3629–39.
23. Yang W, et al. Development and validation of a coagulation-related genes prognostic model for hepatocellular carcinoma. BMC Bioinformatics. 2023;24(1):89.
24. Sun L, et al. Bile acids promote diethylnitrosamine-induced hepatocellular carcinoma via increased inflammatory signaling. Am J Physiol Gastrointest Liver Physiol. 2016;311(1):G91–104.
25. Luo P, et al. A Large-scale, multicenter serum metabolite biomarker identification study for the early detection of hepatocellular carcinoma. Hepatology. 2018;67(2):662–75.
26. Bu L, et al. High-fat diet promotes liver tumorigenesis via palmitoylation and activation of AKT. Gut. 2024;73(7):1156–68.
27. Peng Q, et al. Blood hypercoagulability and thrombosis mechanisms in cancer patients -A brief review. Heliyon. 2024;10(19):e38831.
28. Farrokhi Yekta R, et al. Biomarker Panels Associated with Diagnosis and Overall Survival in Hepatocellular Carcinoma Revealed from Protein-Protein and mRNA-miRNA Interaction Networks. Asian Pac J Cancer Prev. 2025;26(1):249–62.
29. Wang Y, et al. Comprehensive molecular characteristics of hepatocellular carcinoma based on multi-omics analysis. BMC Cancer. 2025;25(1):573.
30. Al-Amodi HS, Kamel HF. Altered Metabolites in Hepatocellular Carcinoma (HCC) Paving the Road for Metabolomics Signature and Biomarkers for Early Diagnosis of HCC. Cureus. 2024;16(10):e71968.
31. Liu X, et al. Multiple Omics data-based biomarker screening for hepatocellular carcinoma diagnosis. World J Gastroenterol. 2019;25(30):4199–212.
32. Zhou Y, et al. ZEB1 enhances Warburg effect to facilitate tumorigenesis and metastasis of HCC by transcriptionally activating PFKM. Theranostics. 2021;11(12):5926–38.
33. Kapelanski-Lamoureux A, et al. Ectopic clotting factor VIII expression and misfolding in hepatocytes as a cause for hepatocellular carcinoma. Mol Ther. 2022;30(12):3542–51.
34. Deshmukh R, Allega MF, Tardito S. A map of the altered glioma metabolism. Trends Mol Med. 2021;27(11):1045–59.
35. Wang M, et al. Lactate dehydrogenase A: a potential new target for tumor drug resistance intervention. J Transl Med. 2025;23(1):713.
36. Peng X, et al. Aging increases susceptibility to liver fibrosis through enhanced NAT10-mediated ac4C modification of TGFbeta1 mRNA. Genome Med. 2025;17(1):90.
37. Zhang S, et al. CAMK2B Impacts the Proliferation, Invasion, and Migration of Glioma Cells via the Ras/Raf/MEK/ERK Signaling Pathway. Oncol Res. 2025;33(10):2961–79.
38. Chen J, et al. Amino acid metabolism in tumor biology and therapy. Cell Death Dis. 2024;15(1):42.
39. Shou Y, et al. Urea cycle dysregulation: a new frontier in cancer metabolism and immune evasion. Cell Commun Signal. 2025;23(1):307.

Publisher's note